



Cite this: *Chem. Sci.*, 2025, **16**, 1093

Received 13th October 2024
Accepted 12th December 2024

DOI: 10.1039/d4sc06957a
rsc.li/chemical-science

Nickel model complexes to mimic carbon monoxide dehydrogenase reactions

Changho Yoo, ^{*ad} Jonghoon Choi, ^{*b} and Yunho Lee, ^{*c}

Biological CO₂/CO interconversion catalyzed at the Ni/Fe heterobimetallic active site of anaerobic carbon monoxide dehydrogenases (CODHs) offers important insights for the design of efficient and selective synthetic catalysts for CO₂ capture and utilization (CCU). Notably, this organometallic C₁ interconversion process is mediated at a three-coordinate nickel site. Extensive research has been conducted to elucidate the redox and structural changes involved in substrate binding and conversion. The CO₂-bound structure of CODH, in particular, has inspired many synthetic studies aimed at exploring key questions, concerning the choice of metal, the role of the unique iron (Fe_u), and the geometry and oxidation states of both Ni and Fe_u, as well as CO₂/CO exchange mechanism. A better understanding of CODH chemistry promises to reveal and uncover fundamental principles for small molecule activation of first-row transition metal complexes. This mini-review focuses on three key aspects: (1) the coordination environment of the Ni centre in CODH, (2) bioinorganic Ni model systems that provide insight into the biological CO₂/CO interconversion at the CODH active site, and (3) recent advances in CODH-inspired catalysis for selective CO₂-to-CO conversion.

1 Introduction

Carbon dioxide conversion is a highly active and multidisciplinary research field, essential for establishing a sustainable chemical industry due to CO₂ being a major byproduct of energy production and petrochemical processes.¹ Moreover, CO₂ plays a critical role in the global carbon cycle (GCC), which is significantly impacted by anthropogenic activities. To restore balance to the GCC, it is crucial to control atmospheric CO₂

^aDepartment of Chemistry, Ulsan National Institute of Science and Technology, Ulsan 44919, Republic of Korea. E-mail: cyoo@unist.ac.kr; Tel: +82 52 217 2694

^bDepartment of Chemistry Education, Chonnam National University, Gwangju 61186, Republic of Korea. E-mail: jonghoon92@jnu.ac.kr; Tel: +82 62 530 2492

^cDepartment of Chemistry, Seoul National University, Seoul 08826, Republic of Korea. E-mail: yunhochem@snu.ac.kr; Tel: +82 2 880 6653

^dGraduate School of Carbon Neutrality, Ulsan National Institute of Science and Technology, Ulsan 44919, Republic of Korea



Changho Yoo

Changho Yoo is an Assistant Professor in the Department of Chemistry at the Ulsan National Institute of Science and Technology (UNIST). He earned his BS and PhD degrees from the Korea Advanced Institute of Science and Technology (KAIST) in 2011 and 2016 under Prof. Yunho Lee. He conducted postdoctoral research with Prof. Alexander J. M. Miller at the University of North Carolina at Chapel Hill (2017–2020). He worked as a senior researcher at the Korea Research Institute of Chemical Technology (2020–2023) before joining UNIST in August 2023. His research focuses on bioinorganic and organometallic chemistry for sustainable catalysis.



Jonghoon Choi

Jonghoon Choi received his PhD degree in the department of chemistry at Korea Advanced Institute of Science and Technology (KAIST) under the supervision of Prof. Yunho Lee in 2020. Then, he was a postdoctoral research associate in Seoul National University (2020–2021) in the same group, followed by a second postdoctoral research position at Humboldt Universität zu Berlin (2021–2022) under the supervision of Prof. Christian Limberg. In 2022, Jonghoon Choi began his independent career as an Assistant Professor at Chonnam National University.



concentration and develop various methods to convert CO_2 into useful chemicals without further CO_2 emissions.^{2–5} Catalytic CO_2 conversion to value-added chemicals, such as formic acid, cyclic carbonates and polycarbonates, has gained considerable attention in recent years. This approach not only helps to reduce the atmospheric greenhouse gas as part of the carbon capture and utilization (CCU) strategies but also supports the development of a sustainable, carbon-neutral chemical industry.

Among the value-added products, carbon monoxide (CO) is one of the most important industrial feedstocks. To efficiently generate CO from CO_2 , numerous transition metal catalysts have been developed. However, many systems face challenges with selectivity and high operating potentials for electrocatalysis.^{6–9} In this context, the selective and efficient conversion of CO_2 to CO, catalyzed by carbon monoxide dehydrogenase (CODH) enzymes, is particularly appealing, because it offers a blueprint for developing transition metal-based CO_2 conversion catalysts.^{10–13} The enzyme employs nickel in the active site, which is incorporated within an iron–sulfur cluster, and it catalyzes reversible interconversion between CO_2 and CO under ambient conditions. According to the recent X-ray crystallographic data, the Ni ion is coordinated by three sulfur donors as a part of the Fe/S cluster.^{14–19} Considering nickel coordination, two distinct geometries are proposed to form during the CO_2 conversion, as illustrated in Fig. 1.

Ligand binding at a three-coordinate nickel centre results in the formation of either a square planar or tetrahedral nickel species, with each geometry associated with a specific spin state (Fig. 1). The square planar geometry generally results in a ligand field that favours a low-spin ($S = 0$) ground state of Ni(II), while the tetrahedral geometry favours a high-spin ($S = 1$) ground state.^{20,21} While distortions away from these two ideal geometries influence the energy of the frontier orbitals, a more significant distortion is required to observe spin state change.²¹ In CODH, structural and spectroscopic studies suggest that the nickel centre predominantly adopts a low-spin state throughout

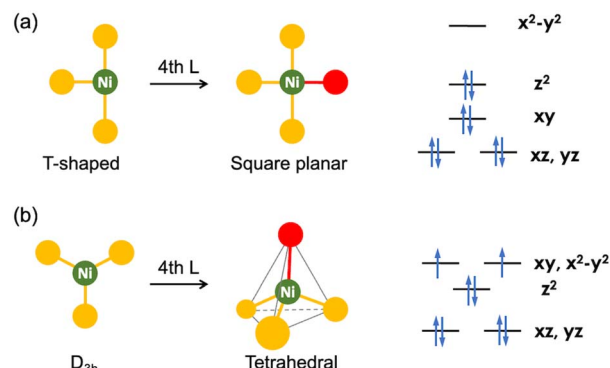


Fig. 1 Two distinct Ni structures: (a) T-shaped and (b) D_{3h} , each supported by three donors. Their reaction with a fourth ligand yields a 4-coordinate species (left) and their Ni(II) electronic structures (right).

the entire catalytic cycle, consistent with the structural data revealing a nearly ideal square planar geometry around Ni.^{14,22–24} Initial studies, however, proposed the possibility of a tetrahedral, high-spin Ni(II) states.^{15,24–26} Thus, it is crucial to examine the structures of CO_2 - and CO-bound Ni species in the different states of CODH to understand how nature facilitates this process. Key questions that arise in understanding CO_2 conversion are: (a) how does CODH enable the catalytic reaction to proceed along a low-energy pathway and (b) why are nickel and iron specifically employed for CO_x conversion ($x = 1$ or 2). By designing synthetic Ni complexes that mimic the coordination environment of the Ni site and certain CO_x -bound intermediate species, one can develop organonickel catalysis for selective CO_2 conversion.

In this review, we will discuss the geometry of the nickel ion as revealed by CODH X-ray structural data and relate these findings to synthetic model complexes. Nickel catalysis in CODH operates as a part of an Fe/S cluster, a component that plays an essential role in both nickel's geometry and electron transfer (ET) processes and cannot be overlooked. Recent studies have explored the structural modelling of the NiFe_4S_4 cluster summarized in other review articles.^{13,27–29} Here, we focus on both structural and functional model compounds, particularly those containing Ni, which bind and mediate the interconversion between CO_2 and CO.

2 Nickel coordination in CODH

Nickel is employed by a bifunctional metalloenzyme, known as carbon monoxide dehydrogenase (CODH)/acetyl CoA synthase (ACS), to facilitate biological organometallic reactions.¹⁰ These reactions include the interconversion of CO₂ to CO at the Ni/Fe site of CODH and C–C and C–S coupling reactions at the single nickel centre in ACS. The X-ray structural data of CODH reported by the Dobbeck group reveal that its active site consists of an open cubane Fe–S cluster equipped with a Ni ion, forming a $[\text{NiFe}_4\text{S}_4]$ core.¹⁶ Two bridging sulfide donors and one cysteine thiolate ligand accommodate a Ni centre, which can form a 4-coordinate nickel species by accepting a fourth ligand, such as CO_2 or CO, as illustrated in Fig. 1. The XRD structural data of



Yunho Lee

Yunho Lee obtained M.S. and PhD degrees from the Johns Hopkins University at Baltimore under the guidance of professor Kenneth D. Karlin. In 2007, he started postdoctoral work with professor Jonas C. Peters at the Massachusetts Institute of Technology and the California Institute of Technology. In 2010, Yunho returned to Korea and started his independent career at KAIST. In spring 2020, he moved his research group to Seoul and currently he is a professor in the Department of Chemistry, SNU. His primary research interest focuses on the small molecule activation inspired by the bioorganometallic chemistry of various metalloenzymes.



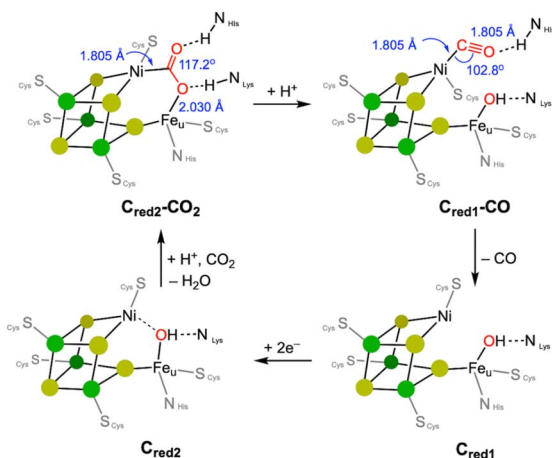


Fig. 2 Proposed catalytic cycle of the CODH. Structural parameters are based on the X-ray crystallographic data.

the intermediate state $C_{red2}\text{-CO}_2$ exhibits a CO_2 molecule is coordinated to the Ni ion *via* a Ni–C bond. One of the O atoms coordinates to the unique Fe center, to give a $\text{Ni}\text{-}\mu\text{-CO}_2\text{-}\kappa\text{C}\text{:}\kappa\text{O-Fe}$ binding mode, as depicted in Fig. 2.^{14,16} In 2015, an atomic-resolution structure of the CO_2 -bound state was reported, showing a Ni–C distance of 1.805 Å, the Fe–O distance of 2.030 Å, and the O–C–O angle of 117.2°, indicating its sp^2 hybridisation.¹⁴

A notable change in the nickel's geometry occurs in the $C_{red2}\text{-CO}_2$ state, which clearly shows a more flattened structure, approaching square planar geometry. Both $\angle S\text{-Ni-S}$ of $\sim 166^\circ$ and $\angle S\text{-Ni-C}$ of 175° are significantly larger than those in the $C_{red1}\text{-CO}$ state; $\angle S\text{-Ni-S}$ of $128\text{-}144^\circ$ and $\angle S\text{-Ni-C}$ of $121\text{-}120^\circ$, as shown in Table 1. The corresponding angles for both C_{red1} and C_{red2} states fall between these states. Enzymes often utilise steric factors and/or secondary coordination sphere, such as H-bonding, to control the metal's geometry, *vide infra*. And CODH also exhibits H-bonding with bound CO_2 , CO and OH ligands.^{10,30} It is difficult, however, to determine whether these

geometrical changes are due to the oxidation state changes accordingly affecting its electronic structure, as depicted in Fig. 1 or are influenced by other factors such as H-bonding, as shown in Fig. 2. Nevertheless, this observation suggests that the NiS_3 core is fairly flexible and that a planar geometry may play a key role in the CO_2 conversion.

The binding mode of CO_2 is particularly interesting, as it may be related to the selective CO generation. Generally, a metal hydride species reacts with CO_2 to form a metal formate species by generating a strong C–H bond, a well-established mechanism with various transition metal catalysts.^{31–33} However, an abnormal insertion mechanism, where CO_2 inserts into the Ni–H bond to form a nickel hydroxycarbonyl species, has been proposed for the CODH reaction, *vide infra*.²⁶ In the case of low-valent metal species that do not involve a metal–hydride bond, direct CO_2 coordination can occur leading to the formation of a metal–COO species, as observed at the Ni site in CODH. Both nickel(1) and nickel(0) states are considered responsible for CO_2 binding, although the reduction potential for the nickel(1/0) couple may be too negative for the biological systems.^{13,16,34–36} The C_{red2} state generated below -500 mV is responsible for reacting with CO_2 .³⁷ Considering the $\text{Ni}(\text{II})\text{-Fe}(\text{II})$ ground state, the two-electron reduction of CO_2 to form a $\text{Ni}(\text{II})\text{-COO-Fe}(\text{II})$ species may involve: (a) fast electron transfer from the Fe/S cluster, or (b) activation of a chemical bond such as Ni–H or Ni–Fe.

After CO_2 is introduced to the active site, protonation occurs, breaking the C–O bond and forming a nickel(II)–CO species. According to biological studies, the CO ligand should be dissociated from the Ni site at this stage, as the π -back-bonding from a Ni(II) ion is weaker compared to lower oxidation states such as Ni(1) and Ni(0).^{38–40} Typically, low-coordinate metal–CO species are fairly stable, which can lead to the deactivation or poisoning of metal catalysts.^{41,42} A notable example is the stability of nickel(0) tetracarbonyl, which plays a key role in the Mond process for producing pure Ni.⁴³ Strong coordination of CO makes it difficult to dissociate from Ni, but it can be weaker when nickel is in its higher oxidation states due to the poor

Table 1 Structural parameters (Å and °) for C clusters at CODH

	C_{red1}	C_{red2}	$C_{red2}\text{-CO}_2$	$C_{red2}\text{-CO}_2$	$C_{red1}\text{-CO}$	$C_{red1}\text{-CO}^a$
$d_{\text{Ni-S}} [\text{\AA}]$	2.07 2.14	2.03 2.16	2.23 2.09	2.198 2.329	2.2 2.3	2.3, 2.3 2.3, 2.4
$d_{\text{Ni-S}_{\text{cys}}} [\text{\AA}]$	2.17	2.17	2.10	2.111	2.3	2.3, 2.3
$d_{\text{Ni-C/O}} [\text{\AA}]$	2.72	2.70	1.96	1.805	2.0	1.7
$d_{\text{Ni-Fe}} [\text{\AA}]$	2.85	2.87	2.76		3.2	3.5/3.6
$d_{\text{CO}} [\text{\AA}]$	—	—	1.25 1.26 1.316	1.298	1.2	1.2
$\angle S\text{-Ni-S} [\text{deg}]$	108.6	109.6	98.4	103.4	110.2	103.1
$\angle S\text{-Ni-S}_{\text{cys}} [\text{deg}]$	93.9 157.4	93.6 156.8	93.2 168.3	90.6 166.0	90.8 143.5	91.2 128.5
$\angle S\text{-Ni-C/O} [\text{deg}]$	78.8 151.8	78.7 148.2	82.3 171.7	100.8 174.9	98.6 125.8	94.3 120.6
PDB	3B53	3B51	3B52	4UDX	3CF4	1OAO
Ref.	16	16	16	14	15	17

^a Two C-clusters were found over two distinct positions.



back-bonding. This suggests that a redox process should be coupled with the CO dissociation from Ni, *vide infra*. The C_{red1} -CO species generated by addition of CO(g) to the C_{red1} state at -100 mV, exhibits five IR vibrational peaks ranging from 1900 to 2074 cm^{-1} , corresponding to Ni-CO stretching vibrations.⁴⁴ The X-ray crystal structure of CODH shows CO binding to the nickel ion in a bent fashion with the Ni-C-O angle of 103° ,¹⁵ as shown in Fig. 2. Although it is uncertain if this structure is directly involved in the catalytic cycle, it suggests that hydrogen bonding may promote this unusual bent Ni-CO coordination, which could be crucial for CO release. The multiple CO vibrations and unusual CO binding make it challenging to fully understand the CO and CO_2 exchange mechanism at the CODH active site.

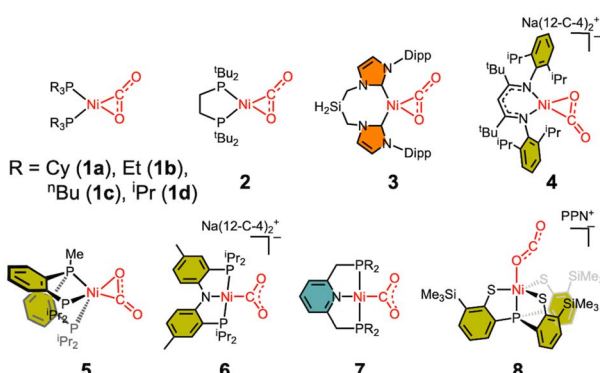
3 Ni- CO_2 structural models

3.1 Ni- CO_2 adducts

The Ni- CO_2 model compounds present how CO_2 binds at the nickel center. These studies provided valuable structural and spectroscopic information about CO_2 -bound nickel complexes, as shown in Scheme 1. The first nickel- CO_2 complex Ni(PCy_3)₂(CO_2) (**1a**) was reported by Aresta and coworkers in 1975.⁴⁵ Analogous Ni(PR_3)₂(CO_2) compounds (**1b** and **1c**) were subsequently reported.^{46,47} In these complexes, the low-coordinate nickel ion is supported by two P donors, allowing both C and O atoms of CO_2 to coordinate to the metal center *via* an η^2 binding mode. Following these initial reports, many other

transition metal- CO_2 compounds were synthesized and examined.^{48,49} The elucidation of the CODH active site structures reported in the 2000s further heightened interest in CO_2 -bound nickel compounds. In the 2010s, nickel- CO_2 compounds supported by monodentate (**1d**) and bidentate (**2**) alkyl phosphine ligands were reported by the Johnson and the Hillhouse groups, respectively.^{50,51} More recently, a similar $\text{L}_2\text{Ni}(\text{CO}_2)$ complex supported by an N-heterocyclic carbene ligand (**3**) was also reported by the Roesler group in 2021.⁵² These η^2 complexes, in which CO_2 binds to the Ni(0) centre, clearly demonstrate activation of the coordinated CO_2 moiety ($d_{\text{C-O}} = 1.22\text{--}1.28$ \AA , $\nu_{\text{CO}_2} = 1695\text{--}1740$ cm^{-1}) compared to the free CO_2 molecule ($d_{\text{C-O}} = 1.16$ \AA , $\nu_{\text{CO}_2} = 2344$ cm^{-1}).^{53,54} Among the $\text{L}_2\text{Ni}\cdot\eta^2\text{-CO}_2$ compounds, the degree of CO_2 activation varies slightly depending on the electron-donating ability of the supporting ligands, see Table 2. The NHC compound **3** exhibits a higher degree of CO_2 activation ($d_{\text{C-O}} = 1.283(4)$ \AA , $\nu_{\text{CO}_2} 1695$ cm^{-1}) compared to the bisphosphine compounds ($d_{\text{C-O}} = 1.22\text{--}1.27$ \AA , $\nu_{\text{CO}_2} = 1721\text{--}1740$ cm^{-1}), due to the stronger electron donation of the NHC donor. In 2024, the Limberg group reported a Ni- $\eta^2\text{-CO}_2$ complex (**4**) supported by an anionic β -diketiminate ligand.⁵⁵ The use of this anionic ligand renders the nickel centre more electron-rich, resulting in the highest level of CO_2 activation observed ($d_{\text{C-O}} = 1.333(3)$ \AA , $\nu_{\text{CO}_2} 1627$ cm^{-1}).

Considering the coordination geometry of the CODH nickel site, the nickel complexes supported by tridentate ligands are particularly intriguing and have been reported relatively recently. In 2014, the Lee group described a Ni- CO_2 compound (**5**) supported by a neutral pincer-type PPP ligand.⁵⁶ Adding one more donor to the L_2Ni core significantly influences CO_2 binding and activation. Although **5** adopts an η^2 binding mode, the Ni-O bond ($2.191(1)$ \AA) is more elongated than in other analogous complexes ($1.90\text{--}1.99$ \AA), due to the presence of an additional donor *trans* to the CO_2 ligand. Compound **5** exhibits a higher degree of CO_2 activation compared to those of **1**-**3** as evidenced by a lower ν_{CO_2} of 1682 cm^{-1} and a longer C-O distance of $1.252(2)$ \AA with an O-C-O angle of 135.1° . Computational analysis reveals that its HOMO displays an antibonding character between Ni and O atoms of CO_2 , supporting its weaker interaction. Interestingly, while all 4-coordinate Ni(CO_2) adducts (**1**-**4**) show planar structures with two donors and both C and O atoms of CO_2 coordinated to Ni, compound **5** exhibits CO_2 binding orthogonally to Ni. Because of this orthogonal binding mode, the interaction between Ni and O weakens.



Scheme 1 Structurally characterized Ni- CO_2 adducts.

Table 2 Physical parameters for structurally characterised Ni- CO_2 complexes (\AA , degrees and cm^{-1})

Binding mode	$d_{(\text{Ni-C})}$	$d_{(\text{Ni-O})}$	$d_{(\text{C-O})}$	$d_{(\text{C-O}')$	$\angle \text{O-C-O}'$	$\nu_{\text{CO}_2\text{asym}}$	
1a	$\eta^2\text{-}\kappa\text{C,O}$	1.84	1.99	1.22	1.17	133	1740
1d	$\eta^2\text{-}\kappa\text{C,O}$	1.842(3)	1.932(2)	1.265(4)	1.211(4)	136.7(4)	1721
2	$\eta^2\text{-}\kappa\text{C,O}$	1.868(2)	1.904(2)	1.266(3)	1.200(3)	138.0(2)	1724
3	$\eta^2\text{-}\kappa\text{C,O}$	1.828(3)	1.949(2)	1.283(4)	1.218(4)	134.6(3)	1695
4	$\eta^2\text{-}\kappa\text{C,O}$	1.834(2)	1.924(2)	1.333(3)	1.172(3)	132.1(2)	1627
5	$\eta^2\text{-}\kappa\text{C,O}$	1.904(1)	2.191(1)	1.252(2)	1.218(2)	135.1(1)	1682
6	$\eta^1\text{-}\kappa\text{C}$	1.911(2)	2.614(1)	1.248(2)	1.247(2)	128.4(2)	1620
7	$\eta^1\text{-}\kappa\text{C}$	1.950(3)	2.721(1)	1.254(3)	1.244(3)	129.3(3)	—
8	$\eta^1\text{-}\kappa\text{O}$	—	2.028(3)	1.132(6)	1.240(7)	171.7(7)	2177



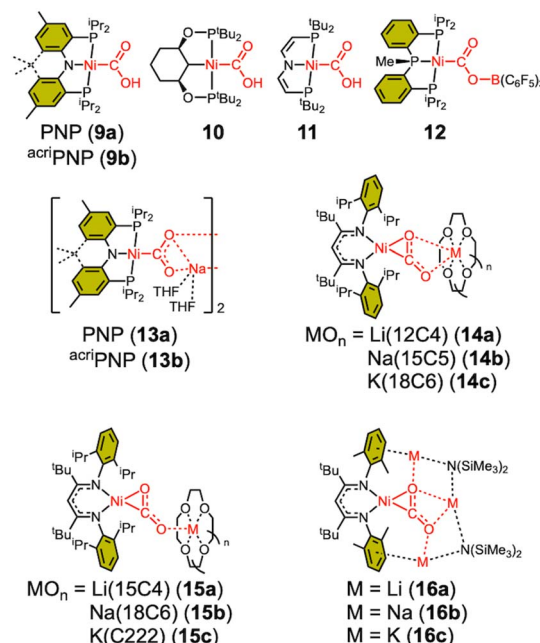
This observation suggests that having three sulfur donors as seen in CODH may be critical for optimal CO_2 activation. Upon the initial coordination of CO_2 to a nickel site, the oxygen atom should be removed from the nickel ion to form a Fe–O bond, as seen in the structure of $\text{C}_{\text{red}2}\text{-CO}_2$. The addition of a Lewis acid such as borane induces an immediate reaction of 5 forming a $\text{Ni}(\text{II})\text{-}\mu\text{-COO-BAr}_3$ adduct, as discussed later.

Further exploration of planar and anionic pincer ligands led to the elongation of a Ni–O bond, resulting in a novel $\text{Ni-}\eta^1\text{-CO}_2$ binding mode. Our group also reported the first example of a $\text{Ni-}\eta^1\text{-CO}_2\text{-}\kappa C$ binding mode by employing a diphosphinoamido (PNP) ligand (6).⁵⁷ X-ray structural data revealed that 6 does not possess any $\text{Ni-O}_{\text{CO}_2}$ bond. Supported by the planar PNP ligand, the nickel center adopts a square planar geometry with two anionic N and C donors aligned *trans* to each other in the *xy* plane. This configuration leads to repulsive interaction between the filled d_{π} orbitals of Ni and two O atoms of the bound CO_2 ligand. The structural parameters of 6 suggest that the CO_2 moiety can be assigned as carbonite (CO_2^{2-}), a 2e^- reduced form of CO_2 .⁵⁸ A similar $\text{Ni-}\eta^1\text{-CO}_2\text{-}\kappa C$ compound (7) was prepared from the CO_2 reaction of a nickel hydride species reported by the Milstein group.⁵⁹ The metal–ligand cooperation of the lutidine-based PNP ligand is essential for facilitating Ni–C bond formation. The structural parameters of 7 are similar to those in 6, reinforcing the idea that the use of a planar ligand is crucial for enhancing CO_2 activation.

As recognized from earlier research involving uranium,⁶⁰ a rare example of an oxygen-bound $\text{Ni-}\eta^1\text{-CO}_2\text{-}\kappa O$ species (8) was reported by the Liaw group in 2016.⁶¹ Compound 8, which exhibits a $\text{Ni-}\eta^1\text{-CO}_2\text{-}\kappa O$ binding mode, stands out from other examples due to its unique binding mode and relatively low degree of CO_2 activation. The O–C–O angle of $171.7(7)^\circ$ indicates minimal activation of CO_2 , Table 2. The bond angles and distances of the CO_2 moiety are closely aligned with those observed in the free CO_2 molecule. Although the XAS study suggests 8 possesses a $\text{Ni}(\text{III})\text{-}(\text{CO}_2^{*})$ character, the bond lengths, angle and stretching frequency clearly indicate that CO_2 activation is relatively low compared to other Ni-CO_2 compounds, likely due to the limited reducing power of $\text{Ni}(\text{II})$ in this example.

3.2 $\text{Ni-CO}_2\text{-LA}$ (Lewis acid) adducts

The CO_2 -bound structure of CODH reveals that the CO_2 moiety interacts with both Fe_u and Lys563 through one O atom, while another interaction occurs with His93, as shown in Fig. 2.^{14,16} These interactions with Fe and protein residues are believed to contribute significantly to CO_2 activation.^{30,62} The influence of such interactions can be inferred from model studies. To replicate similar interactions with a bound CO_2 moiety, nickel complexes with Lewis acids such as proton, borane, alkali cation, and transition metal have been synthesized using various approaches. In 2013, our group firstly reported a nickel hydroxycarbonyl (9a) species, a proton adduct of a nickel CO_2 compound, Scheme 2.⁶³ With a PNP ligand, 9a was prepared through CO insertion into the corresponding nickel hydroxyl compound. A similar nickel hydroxycarbonyl species (9b) was



Scheme 2 Selected $\text{Ni-CO}_2\text{-LA}$ adducts.

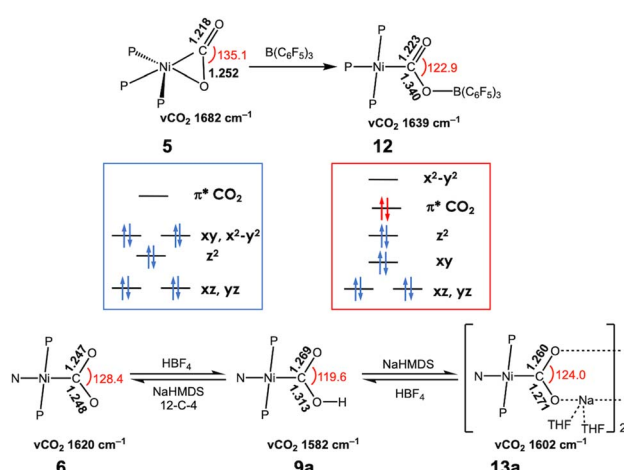
also prepared using an acridane-based PNP ligand, showing comparable physical parameters, see Table 3.³⁹ Another nickel hydroxylcarbonyl compound 10 was also prepared by carbonylation reported by the Wendt group in 2018.⁶⁴ The Schneider group reported the synthesis of 11 from the reaction of a nickel hydride species with CO_2 under photochemical conditions, *vide infra*.⁶⁵ All hydroxycarbonyl species (9–11) exhibit a $\text{Ni}(\text{II})\text{-CO}_2^{2-}$ character.

As a borane adduct, a $\text{Ni-COO-B(C}_6\text{F}_5)_3$ species (12) was prepared from addition of $\text{B(C}_6\text{F}_5)_3$ to a $\text{Ni-}\eta^2\text{-CO}_2$ compound (5), reported in 2015.⁵⁶ Due to the support from a neutral PPP ligand, the level of CO_2 activation is relatively weak compared to other examples, see Table 3. This can be attributed not only to the charge effect (anionic *vs.* neutral donor as the central moiety) but also to the planarity of the pincer ligand. The PPP ligand is not ideally suited to accommodate a square planar geometry, as evidenced by $\angle \text{P-Ni-P}$ of $154.43(4)^\circ$ in 12. Compound 5 and 12 offer a direct comparison between Ni-CO_2 and $\text{Ni-CO}_2\text{-LA}$ adducts. The incorporation of Lewis acidic borane significantly alters the degree of CO_2 activation. Specifically, the C–O distance is elongated from $1.252(2)$ Å to $1.340(4)$ Å and ν_{CO_2} values shift from 1682 cm^{-1} to 1639 cm^{-1} . These changes indicate that upon addition of borane, the nickel-bound CO_2 is clearly converted to carbonite (CO_2^{2-}), as shown in Fig. 3. The negative charge on the oxygen atom is stabilized by the Lewis acidic borane, resulting in a shift in the binding mode from η^2 to $\mu^2\text{-}\kappa C\text{:}\kappa O$. This transformation highlights how both structural changes and the Lewis acid effect can induce a two-electron transfer from $\text{Ni}(0)$ to the bound CO_2 . As anticipated, structural change to a square planar geometry increases the energy of the $d_{x^2-y^2}$ orbital. If its energy surpasses that of π^* orbital of CO_2 , carbonite formation occurs, as depicted in Fig. 3. Similar nickel carbonite adducts with alkali metal cations are



Table 3 Physical parameters for selected Ni–CO₂–LA complexes (Å, degrees and cm^{−1})

LA	Binding mode	<i>d</i> _(Ni–C)	<i>d</i> _(C–O)	<i>d</i> _(C–O')	∠ O–C–O'	<i>v</i> _{CO₂asym}	
9a	H	μ ₂ –κC:κO	1.866(2)	1.313(3)	1.269(3)	119.6(2)	1582
9b	H	μ ₂ –κC:κO	1.859(1)	1.338(2)	1.244(2)	119.3(1)	1579
10	H	μ ₂ –κC:κO	1.899(4)	1.299(5)	1.297(5)	117.5(4)	—
11	H	μ ₂ –κC:κO	1.854(2)	1.299(3)	1.274(3)	119.5(2)	1584
12	B	μ ₂ –κC:κO	1.923(3)	1.340(4)	1.223(4)	122.9(3)	1639
13a	Na	μ ₃ –κC:κO, O':κO	1.882(1)	1.271(1)	1.260(1)	124.0(1)	~1602
13b	Na	μ ₃ –κC:κO, O':κO	1.889(2)	1.262(2)	1.261(2)	123.5(2)	1533
14a	Li	μ ₂ –κC ₂ O:κO':κO''	1.828(4)	1.291(6)	1.192(6)	127.8(5)	1630
14b	Na	μ ₂ –κC ₂ O:κO':κO'	1.855(2)	1.281(3)	1.209(3)	133.2(2)	1600
14c	K	μ ₂ –κC ₂ O:κO':κO'	1.890(6)	1.231(9)	1.22(1)	144.0(8)	1621
15a	Li	μ ₂ –κC ₂ O:κO':κO'	1.799(3)	1.263(4)	1.216(4)	131.6(3)	1621
16a	Li	μ ₄ –κC ₂ O:κO, O':κO:κO	1.786(4)	1.275(5)	1.235(5)	128.0(4)	1616

Fig. 3 Comparison of Ni–CO₂ and Ni–CO₂–LA adducts.

also known. Our group reported sodium nickel-carbonate adducts (**13a** and **13b**) through the deprotonation of corresponding hydroxycarbonyl species.^{39,57,63} Interestingly, the Limberg group recently reported a series of Ni–CO₂–LA adducts with Li, Na and K ions in the presence of polyether co-ligands (**14** and **15**), synthesized *via* deprotonation of corresponding formate species.^{55,66,67} Table 3 summarises the physical parameters for selected Ni–CO₂–LA adducts.

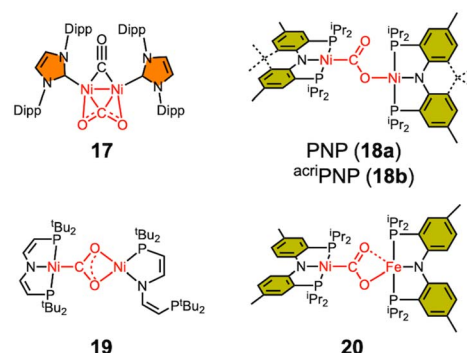
A comparison between **6**, **9a**, and **13a** further highlights the influence of proton and alkali metal cation on CO₂ activation, as shown in Fig. 3. The addition of a proton notably increases the C–O distance of the protonated oxygen atom from 1.247(2) to 1.313(3) Å. The other C–O bond also elongates slightly from 1.248(2) to 1.269(3) Å, likely due to the H-bonding interactions within a dimeric solid-state structure. Similarly, the sodium cation in **13a** promotes CO₂ activation, with C–O bonds elongated to 1.260(1) and 1.271(1) Å. Both C–O bonds exhibit comparable lengths as the sodium cation interacts with both O atoms in a dimeric form. The C–O bond elongation and IR shift (~1602 cm^{−1}) in **13a** are less significant than in **9a**, this is presumably due to the lower Lewis acidity of sodium cations. These examples underscore how Lewis acid, such as proton,

borane, and alkali metals, can stabilize carbonate (CO₃^{2−}), thereby enhancing CO₂ activation.

The Limberg group systematically investigated the impact of the distance, number and nature of cations by preparing a series of Ni–CO₂–LA adducts with different cations and polyether co-ligands (**14**–**16**).^{55,66,67} A comparison of cations (**14a**–**c**) with the same μ₂–κC₂O:κO':κO'' binding mode reveals that the degree of CO₂ activation follows the trend Li > Na > K based on stretching frequencies and ¹³C NMR chemical shifts of CO₂ of 170.34 (**14a**), 168.58 (**14b**) and 167.59 (**14c**) ppm. This trend can be attributed to the higher Lewis acidity of lighter ions. Furthermore, the spatial separation, which varies with a different co-ligands, was also evaluated. Increasing the size of the macrocycle results in a detachment of the cation from the Ni–CO₂ in **15a**–**c**, leading to weaker CO₂ activation. Conversely, increasing the number of cation interactions enhances CO₂ activation observed in **16a**–**c**.

3.3 Bimetallic Ni–CO₂–TM (transition metal) adducts

Only a limited number of bimetallic Ni–CO₂–TM species have been reported in the literature (Scheme 3). In 2007, the Sadighi group reported a bimetallic Ni–CO₂ compound (**17**) supported by an NHC ligand, where CO₂ is bound as a bridging ligand between two nickel ions in a μ-η²,η² fashion.⁶⁸ Although the binding mode of CO₂ in **17** differs significantly from that observed in the CODH chemistry, **17** can still be considered as

Scheme 3 Reported Ni–CO₂–TM adducts.

an early example of a dinuclear nickel CO_2 adduct. In 2013, our group reported a dinickel $\text{Ni}-\text{CO}_2-\text{Ni}$ compound (**18a**), which adopts a $\mu^2\text{-}\kappa C:\kappa O$ binding mode, reminiscent of that of CO_2 in the CODH active site.⁶³ This species was synthesized by reacting **9a** with (PNP)NiOH. A similar compound (**18b**) with the ${}^{\text{aci}}\text{PNP}$ ligand was synthesized by reacting a ${}^{\text{aci}}\text{PNP}\text{Ni}(\text{i})$ species with CO_2 .⁶⁹ The degree of CO_2 activation in **18a** is comparable to that in **9a**, as indicated by the C–O distances (1.296(3) and 1.240(3) Å), the O–C–O angle of 123.7(2)° and the CO_2 asymmetric stretching frequency of 1518 cm^{-1} . A similar dinickel compound **19** was prepared by the Schneider group through a photo-induced reaction of a nickel hydride species with CO_2 .⁶⁵ Mechanistic studies revealed that the $\text{Ni}(\text{i})$ species is formed during the photochemical reaction. The bridging CO_2 moiety in **19**, where both O atoms are coordinated to a single nickel ion, differs from that in **18**, likely due to the flexibility of the PNP ligand in **19**, which permits the de-coordination of one of the P donors.

Considering the CODH active site, only one example of a $\text{Ni}-\text{CO}_2-\text{Fe}$ adduct has been reported. Our group reported a $\text{Ni}-\text{CO}_2-\text{Fe}$ compound (**20**), which was prepared from condensation between **9a** and (PNP)FeOH.⁵⁷ Its C–O distances are 1.269(2) and 1.289(2) Å, which are consistent with those in other bimetallic CO_2 adducts, see Tables 3 and 4. This indicates that the iron ion acts as a typical Lewis acid. However, this does not necessarily imply that the CO_2 binding and activation involving structural and redox changes are solely related to Ni. To address such a question, Ni–Fe bimetallic complexes have previously been synthesized and studied,⁷⁰ but none exhibited CODH-like activity. A redox-active Fe ion likely plays a crucial role in CO_2 activation, a hypothesis that remains to be evaluated.

3.4 Lessons from model compounds

The structural and spectroscopic data offer valuable insights into CO_2 binding and its level of activation. While $\eta^2\text{-}\text{CO}_2$ compounds (**1–5**) exhibit a lower degree of CO_2 activation assigned as $\text{Ni}(\text{0})\text{-}(\text{CO}_2)$, other bridging CO_2 compounds (**9–20**) possessing a single Ni–C bond present a higher degree of CO_2 activation, which can be assigned as $\text{Ni}(\text{II})\text{-CO}_2^{2-}$. This suggests that the CO_2 -bound active site of CODH can be conceptualized as a $\text{Ni}(\text{II})\text{-}(\text{CO}_2^{2-})\text{-Fe}$ species based on its binding mode and structural parameters. A series of nickel model systems disclose the design principles underlying the CODH active site. Comparisons between monodentate (**1a–d**), bidentate (**2–4**),

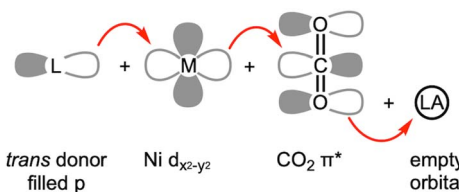


Fig. 4 Frontier orbitals involved in CO_2 activation.

and tridentate ligands (**5–7**) indicate that the tridentate ligands are more effective than two-donor systems in CO_2 activation. The presence of an additional donor increases electron density at the nickel center, thereby facilitating further reduction of CO_2 . Moreover, the geometry imposed by the ligand plays a crucial role. As illustrated in Fig. 1 and 3, three donors create a situation where a $\text{Ni} d_{x^2-y^2}$ orbital increases in energy relative to other d orbitals. This allows for electron transfer to the $\text{CO}_2 \pi^*$ orbital. When the ligand supports a square planar environment (**6** and **7**), the donors can direct more electron density toward the $\text{Ni} d_{x^2-y^2}$ orbital, enabling bond formation with $\text{CO}_2 \pi^*$ orbital (Fig. 4). Through this bonding interaction, two electrons are transferred from Ni to CO_2 , reducing it to a carbonite (CO_2^{2-}) form. Furthermore, as previously discussed, three donors can create an electronic structure that weakens the bond between Ni and O of bound CO_2 . The Lewis acid interaction (**12**, **13** and **14**) not only promotes inner-sphere electron transfer from the Ni ion during the initial stage of CO_2 binding but also stabilizes the negative charge on the carbonite oxygen by accepting electron density through its empty orbital. A comprehensive evaluation of the model $\text{Ni}-\text{CO}_2-\text{LA}$ compounds listed in Tables 2 and 3 reveals that the ancillary ligand plays a more significant role in CO_2 activation than the Lewis acid. Thus, the degree of CO_2 activation is primarily governed by the choice of the ancillary ligand, while the Lewis acid serves a supplementary role.

4 Reactivity of model $\text{Ni}-\text{CO}_2$ compounds

4.1 Formation of $\text{Ni}-\text{CO}_2$ adducts

In CODH, the $\text{C}_{\text{red}2}$ state is responsible for CO_2 binding, leading to the formation of the $\text{Ni}-\text{COO-Fe}$ species. The $\text{C}_{\text{red}2}$ state is generally thought to involve a low-valent nickel ion, such as $\text{Ni}(\text{0})$ or $\text{Ni}(\text{i})$, but there remains ongoing debate regarding its

Table 4 Physical parameters for structurally characterized $\text{Ni}-\text{CO}_2-\text{TM}$ complexes (Å and degrees)

	TM	CO_2 binding mode	$d_{(\text{Ni}-\text{C})}$	$d_{(\text{C}-\text{O})}$	$d_{(\text{C}-\text{O}^{'})}$	$\angle \text{O}-\text{C}-\text{O}^{'}$	$\nu_{\text{CO}_2\text{,asym}}$
17	Ni	$\mu^2\text{-}\kappa C:\kappa O:\kappa C:\kappa O^{'}$	1.952(2)	1.255(2)	1.257(2)	133.4(1)	1630
18a	Ni	$\mu^2\text{-}\kappa C:\kappa O$	1.888(2)	1.296(3)	1.240(3)	123.7(2)	1518
18b	Ni	$\mu^2\text{-}\kappa C:\kappa O$	1.94(2) ^a	1.34(2) ^a	1.22(1) ^a	122(1) ^a	1511
			1.94(1) ^a	1.24(2) ^a	1.24(1) ^a	121(1) ^a	
19	Ni	$\mu^2\text{-}\kappa C:\kappa O,O^{'}$	1.875(3) ^b	1.292(3) ^b	1.280(3) ^b	114.0(2) ^b	1584
			1.869(3) ^b	1.291(3) ^b	1.285(3) ^b	114.1(2) ^b	
20	Fe	$\mu^2\text{-}\kappa C:\kappa O,O^{'}$	1.858(1)	1.289(2)	1.269(2)	116.5(1)	1510

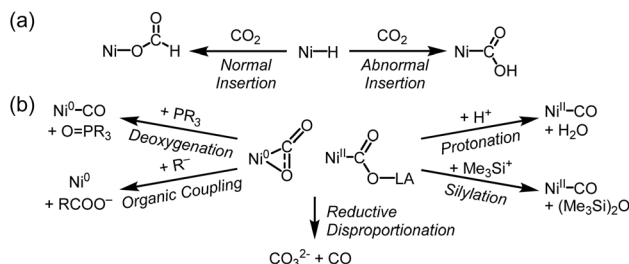
^a The CO_2 moiety was disordered over two distinct positions. ^b Asymmetric unit cell contains two molecules of **18**.



oxidation state. Alternative possibilities, such as Ni(i) or Ni(n)-H species, have also been proposed.^{26,34-36} A critical question remains: which nickel oxidation state is capable of reacting with CO₂ under biological conditions.^{13,16,34-36} To address this, various synthetic efforts have led to the preparation of several Ni-CO₂ compounds, offering chemical insights into the proposed CO₂ activation mechanisms.

Aresta's first Ni-CO₂ compound (**1**) was synthesized by CO₂ addition to (PCy₃)Ni(N₂). Other Ni(0)- η^2 -CO₂ compounds have also been prepared from Ni(0) precursors possessing a coordinating N₂ or a solvent molecule. The five-coordinate Ni- η^2 -CO₂ compound **5** was prepared from $\{(\text{PP}^{\text{Me}}\text{P})\text{Ni}^0\}_2(\mu\text{-N}_2)$. Although the degree of CO₂ activation in **5** is low, the addition of a Lewis acid leads to the formation of **12** possessing a Ni(II)-CO₂²⁻ moiety. This may mimic the initial CO₂ binding at the CODH nickel center and subsequent stabilization with Fe_u. As a notable example, our group reported the first instance of CO₂ binding at a Ni(0)-CO species (**A**) with the expulsion of CO, as illustrated in Fig. 5a.³⁹ By employing a rigid ^{acri}PNP ligand, Ni(0)-CO rapidly reacts with CO₂ at room temperature, leading to the selective generation of a Ni(II)-carbonate species **13b**. In contrast, a (PP^{Me}P)Ni(0)-CO species supported by a neutral PP^{Me}P ligand does not react with CO₂ due to thermodynamic reasons ($\Delta G = +20$ kcal mol⁻¹). However, the corresponding (PP^{Me}P)Ni(CO₂) species (**5**) can be formed from the corresponding Ni(0)-N₂ species.⁴⁰ This demonstrates that the structural preference of the tridentate ligand supporting either square planar or tetrahedral geometry influences the thermodynamics of the reaction.

The reaction of Ni(i) with CO₂ has been recently investigated. In 2017, our group reported a metalloradical species (^{acri}PNP)Ni(i), that reacts with CO₂ to produce the dinickel carbonite compound $\{(\text{acriPNP})\text{Ni}\}_2(\mu\text{-CO}_2)$ (**18b**) *via* cooperative binuclear



Scheme 4 (a) Normal and abnormal insertion of CO₂ into nickel hydride species. (b) Common reactions found in Ni-CO₂ adducts.

reduction.⁶⁹ A similar reaction involving Ni(i) leading to the formation of dinickel carbonite **19** was also reported by the Schneider group.⁶⁵ Both reactions of Ni(i) with CO₂ occur almost instantaneously at room temperature, indicating that two Ni(i) species cooperatively undergo a single-electron transfer pathway with a low activation barrier for both binding and reduction of CO₂. In CODH, a comparable reaction route may be facilitated by electron transfer from the Fe/S cluster or Fe_u to a Ni(i) ion during the CO₂ binding.

Several recent studies have highlighted these reactions involving a nickel-hydride species and CO₂ can lead to unusual transformation to give a nickel-carbonite species, referred to as "abnormal" insertion (Scheme 4a). These reactions, however, typically require photolysis, strong base, or metal-ligand cooperative transformation.^{59,65-67} In 2013, our group reported that the thermolysis of (PNP)Ni-COOH (**9a**) resulted in producing a nickel hydride species with ~35% yield.⁶³ Although the reverse reaction was not observed with (PNP)NiH, this suggests the potential for abnormal insertion based on the microscopic reversibility. In 2018, the Schneider group provided the first instance of abnormal insertion forming a hydroxycarbonyl species **11** under photochemical conditions.⁶⁵ This study demonstrates that to access a nickel carbonite species, the transformation of a nickel hydride species requires high energy light ($\lambda > 305$ nm) to overcome a 35 kcal mol⁻¹ energy barrier. In contrast, the formation of formate proceeds with a relatively lower barrier of 25 kcal mol⁻¹. Mechanistic studies revealed that the irradiation promotes N-H reductive elimination to form a Ni(0) species, which subsequently reacts with CO₂ to produce **11**. The Limberg group reported deprotonation of a nickel-formate species to generate a corresponding nickel carbonite (**14-16**).^{66,67} Since formate can be readily generated by normal CO₂ insertion into Ni-H, this result implies that CO₂ may react with a Ni-H bond at the active site. Another approach was presented by the Milstein group, reporting the formation of a Ni(II)- η^1 -CO₂- κ C compound (**7**) from the reaction of nickel(II) hydride with CO₂ *via* metal-ligand cooperation.⁵⁹ Hydride transfer involving aromatization and dearomatization of the lutidine-based PNP ligand enables the generation of the Ni-CO₂ compound from nickel hydride.

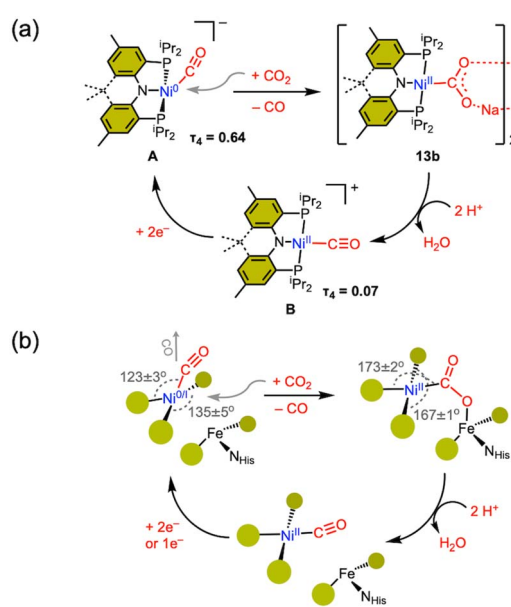


Fig. 5 (a) Synthetic cycle for CO₂ to CO in the (^{acri}PNP)Ni system. (b) Proposed CODH mechanism based on the model study; bond angles are based on Table 1.

4.2 Conversion of Ni-CO₂ to Ni-CO

The reactivity of Ni-CO₂ adducts is summarized in Scheme 4b. Early studies on Ni(0)- η^2 -CO₂ compounds reported the



deoxygenation of CO_2 using internal or external phosphine, resulting in the formation of $\text{Ni}(0)\text{-CO}$ and phosphine oxide.^{50,51,59} Aresta's complex **1a** was employed as a $\text{Ni}(0)$ precursor and catalyst for organic coupling reactions.^{71,72} The Dong group also reported a CO_2 coupling reaction with an organozinc reagent to produce carboxylic acid.⁷³ Reductive disproportionation has been observed, where two CO_2 molecules are converted to CO_3^{2-} and CO *via* electron transfer.^{45,65,66,68,74}

To mimic the CODH reaction, protonation of Ni-CO_2 compounds was investigated. Protonation of **1a** was attempted with PhSH . Although $(\text{PCy}_3)_2\text{Ni}(\text{CO})_2$ was obtained, a nickel hydride species was formed accompanied by the elimination of CO_2 at room temperature.⁷⁵⁻⁷⁷ In contrast, protonation of $\text{Ni}(\text{II})\text{-CO}_2$ compounds yields $\text{Ni}(\text{II})\text{-CO}$ in high yield without any evidence of hydride formation. Our group reported that the protonation of a hydroxycarbonyl species (**9a** and **9b**) produced $\text{Ni}(\text{II})\text{-CO}$ and H_2O in high yield of >90%.⁶³ This result is somewhat distinctive compared to the result of $(\text{PP}^{\text{Me}}\text{P})\text{Ni}(\text{CO}_2)$ (**5**). Due to the weak activation of CO_2 , **5** is converted back to $\{(\text{PP}^{\text{Me}}\text{P})\text{Ni}^{10}\}_2(\mu\text{-N}_2)$ under a N_2 atmosphere. Protonation of another $\text{Ni}(\text{II})$ carbonite compound (${}^{\text{acri}}\text{PNP}\text{NiCOO-Na}$ (**13b**)) also produces $\text{Ni}(\text{II})\text{-CO}$ in high yield of 93% *via* a hydroxycarbonyl intermediate. As a related example, silylation of a $\text{Ni}(\text{II})\text{-CO}_2\text{-Li}$ compound (**16a**) also gave Ni-CO .⁶⁷ These studies demonstrate that the oxidation state and the degree of CO_2 activation significantly influence reactivity.

4.3 CO elimination and completion of the cycle

As the final step of CO_2 conversion, the product CO should be eliminated from the nickel center. According to the current proposed mechanism, CO should be removed from a $\text{Ni}(\text{II})$ state, due to the poor back donation to the CO ligand.³⁸⁻⁴⁰ At lower oxidation states, such as $\text{Ni}(\text{i})$ or $\text{Ni}(0)$, in general, a nickel carbonyl species do not react with CO_2 , as back-donation stabilizes the Ni-CO species. As expected, $(\text{PP}^{\text{Me}}\text{P})\text{Ni-CO}$ does not react with CO_2 .⁴⁰ However, the CO_2 reaction of $\{(\text{PP}^{\text{Me}}\text{P})\text{Ni}^{10}(\text{CO})\}^-$ revealed immediate transformation to various products, including carbamate, carbonate, and carbonyl species.⁷⁸ After this undesired result, our group successfully increased the selectivity of the CO_2 reaction with a nickel(0)-CO species by employing a structurally rigidified ligand.³⁹ The newly designed ${}^{\text{acri}}\text{PNP}$ ligand (${}^{\text{acri}}\text{PNP}^- = 4,5\text{-bis}(\text{diisopropylphosphino})-2,7,9,9\text{-tetramethyl-9H-acridin-10-ide}$) effectively accommodates a square planar nickel(II) center, revealing unusual structural features due to its rigid backbone.⁶⁹ Interestingly, two-electron reduction effectively alters the geometry of $[{}^{\text{acri}}\text{PNP}\text{Ni}^{10}\text{-CO}]^-$ (**A**), causing the CO ligand to shift towards an axial position. This change opens the binding site for CO_2 , as depicted in Fig. 5a. This structural change facilitates the selective generation of a $\text{Ni}(\text{II})$ -carbonite species (**13b**) from the CO_2 reaction of **A** with the expulsion of CO . This process could be closely related to the CODH mechanism and the positioning of both CO and CO_2 channels, as illustrated in Fig. 5b.^{17,79-81} After the CO_2 binding to the nickel center, subsequent protonation can cleave the C-O bond to give a $\text{Ni}(\text{II})\text{-CO}$ species (**B**). A two-

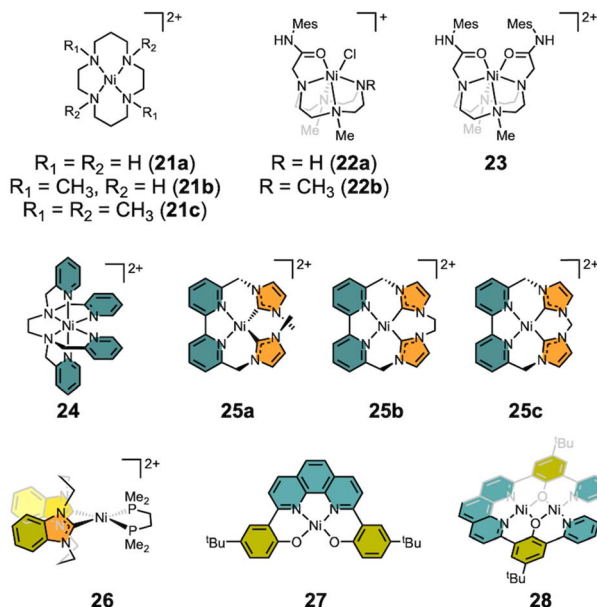
electron reduction of $\text{Ni}(\text{II})\text{-CO}$ completes a closed synthetic cycle for CO_2 reduction to CO at a single nickel center, as shown in Fig. 5a.

Based on the $({}^{\text{acri}}\text{PNP})\text{Ni}$ scaffold, the synthetic COCH_2 reduction cycle encompasses the following features, as illustrated in Fig. 5a. (1) Reduction of the nickel center systematically alters the position of the CO ligand (from *equatorial* to *axial*), thereby opening a CO_2 binding site. (2) CO liberation occurs upon CO_2 coordination to a nickel(0) center, which oxidizes Ni and reduces the back-bonding to CO . (3) Structural change of $\text{Ni}(\text{II})$ to a square planar geometry, along with the cationic Lewis acid interaction facilitate the formation of a $\text{Ni}(\text{II})$ -carbonite species. (4) Protonation of the carbonite moiety cleaves the C-O bond to produce a Ni-CO species. Finally, (5) reduction of nickel-CO may occur at a more positive reduction potential, approximately -1.2 V *vs.* Fc/Fc^+ . These findings offer chemical insights that may help elucidate the organonickel chemistry of the CODH active site. As depicted in Fig. 5b, we may propose an alternative CODH mechanism. The coordination geometry about the nickel center in CODH aligns fairly well with the nickel species generated with an $({}^{\text{acri}}\text{PNP})\text{Ni}$ scaffold, as illustrated in Fig. 5. In particular, the S-Ni-S angles differ significantly between Ni-CO and Ni-CO_2 , as listed in Table 1. The reduction potential of the nickel site, which is connected to a Fe-S cluster, is particularly considered. Although a bound CO ligand generally reduces the reactivity of a Ni-CO species, it can significantly and positively shift the reduction potential, aiding electron transfer to the nickel center. In the case of an $({}^{\text{acri}}\text{PNP})\text{Ni}$ scaffold, the reduction potential of a $\text{Ni}(\text{II})\text{-CO}$ species is ~ 1 V more positive than that of $({}^{\text{acri}}\text{PNP})\text{Ni}^{10}\text{-Cl}$. This demonstrates the influence of a π -acidic CO ligand compared to a π -basic X-type ligand in the reduction of a nickel(II) complex. Thus, we propose one or two electron reduction of the Ni ion should occur when CO is bound, as illustrated in Fig. 5b. Given the complex nature of the CODH active site, applying this model directly to its mechanism may be challenging. However, both reduction potential and the positioning of the CO/CO_2 channels should be carefully considered. Interestingly, the mechanism suggested by our model study is in line with recent proposals based on calculations and kinetic studies with CODH.^{34,82,83}

5 CODH functional models

There are numerous examples of electrocatalytic CO_2 conversion based on transition metals.⁶⁻⁹ Some systems have adopted strategies inspired from CODH, such as hydrogen bonding in the secondary coordination sphere and bimetallic approaches.^{6,84,85} These include not only molecular catalysts but also heterogeneous catalytic systems and photocatalysis, which are beyond the scope of this review. This section focuses on molecular nickel catalysts for the electrocatalytic CO_2 reduction. Seminal works by the DuBois,⁸⁶ Lehn⁸⁷ and Kubiak groups^{88,89} have demonstrated electrocatalytic CO_2 conversion to CO , involving the formation of a M-COO^- intermediate, reminiscent of CODH chemistry. Only the DuBois group's work exhibits a bimetallic pathway. Most of the nickel electrocatalytic systems





Scheme 5 Functional models of CODH.

discussed below and highlighted in Scheme 5 proceed through the reductive transformation of CO_2 to CO *via* the formation of a nickel metallacarbonite species, as a proposed intermediate.

Nickel catalysts supported by macrocyclic ligands were explored early on. In 1984, the Sauvage group investigated the electrocatalytic CO_2 reduction using $\text{Ni}(\text{cyclam})\text{Cl}_2$ (21a) (cyclam: 1,4,8,11-tetra-azacyclotetradecane), as shown in Scheme 5.⁹⁰ The catalysis was carried out at -1.0 V (vs. NHE) in water yielding selective CO production with a current efficiency of 99% and $\text{TOF} = 18 \text{ h}^{-1}$. A unique feature of this system is that the active nickel catalyst adsorbs onto the Hg working electrode, whereas 21a tends to promote hydrogen evolution in the aqueous solution. When the same reaction was conducted using a glassy carbon electrode, lower faradaic efficiencies (FE) were observed due to hydrogen evolution.⁹¹ In 2023, the Cowan group incorporated the pulsed electrolysis, with asymmetric anodic pulse ranging from 40 ms to 1 s, throughout electrolysis on 21a. This approach resulted in a 4-fold increase in selectivity for CO production ($\text{CO}/\text{H}_2 = 2.42 \pm 0.10$). XPS analysis on the glassy carbon electrode surface suggested that standard electrolysis causes catalyst degradation through cyclam loss and the deposition of $\text{Ni}(0)$ carbonyl species on the electrode surface enhances hydrogen evolution.⁹² Similarly, the Rosenthal group reported electrocatalytic CO_2 reduction using a nickel(II) cyclen complex (22, cyclen: 1,4,7,10-tetraazacyclododecane).⁹³ The catalytic reaction was conducted in MeCN achieving a FE of up to $78 \pm 5\%$ with $[\text{Ni}(\text{TrMCy}^{\text{Mes}})\text{Cl}]\text{Cl}$ (22b) ($\text{TrMCy}^{\text{Mes}}$: 1,4,7-trimethyl-10-acetamide^{Mes}-1,4,7,10-tetraazacyclododecane) at -1.95 V vs. SCE (-2.33 V vs. Fc/Fc^+).⁹⁴ The electrocatalytic process undergoes two-electron reduction coupled with the chloride extrusion, which is presumably a prerequisite for CO_2 coordination. The importance of an unmasked coordination site was highlighted by modifying $\text{TrMCy}^{\text{Mes}}$ to 1,7-dimethyl-4,10-bis(acetamide^{Mes})-1,4,7,10-tetraazacyclododecane

($\text{DMCy}^{\text{2Mes}}$).⁹⁴ Under the same conditions at -1.95 V (vs. SCE, -2.33 V vs. Fc/Fc^+), $[\text{Ni}(\text{DMCy}^{\text{2Mes}})](\text{PF}_6)_2$ (23) exhibited a low catalytic faradaic efficiency of $24 \pm 4\%$, as the two amide arms interfere with CO_2 coordination.

In 2018, the Machan group reported the electrocatalytic CO_2 reduction mediated by $[\text{Ni}(\text{TPEN})](\text{PF}_6)_2$ (24) (TPEN = *N,N,N',N'*-tetrakis(2-pyridylmethyl)ethylenediamine).⁹⁵ Using foot-of-the-wave (FOWA) analysis, the divalent nickel catalyst demonstrated a TOF_{max} of $7.72 \times 10^8 \text{ s}^{-1}$ in the presence of 2.50 M phenol as a proton source, a remarkable result compared to other systems exhibiting TOFs ranging from 4 to 47.5 s^{-1} . Compared to 22 and 23, the weaker pyridine donors in 24 enable a milder operation potential of -2.05 V, compared to the stronger aliphatic amine donor (-2.33 V vs. Fc/Fc^+). Unfortunately, 24 undergoes significant degradation to $\text{Ni}(\text{CO})_4$, likely due to the weak field donors within the TPEN ligand, leading to ligand loss during the catalysis. Consequently, CO scavenger 21c is necessary to prolong the catalyst lifetime.

In 2018, Panetier and Jurss reported electrocatalytic CO_2 reduction using a series of nickel complexes supported by bipyridyl-N-heterocyclic carbene donors (25), as shown in Scheme 5.⁹⁶ These nickel complexes were prepared with the ligands generated from the reaction of 6,6'-bis(bromomethyl)-2,2'-bipyridine alkylated with 1-methylimidazole (25a) or diimidazoles (25b and 25c). Structural analysis of 25a-c reveals that both 25b and 25c adopt a square planar geometry ($\tau_4 = 0.11$ and 0.08, respectively), while 25a exhibits noticeable distortion at the Ni center ($\tau_4 = 0.26$) due to the two methyl groups. All nickel complexes display high FE of 98–99% at approximately -2.4 V vs. Fc/Fc^+ . However, the selectivity and TOF for CO generation increase from 5% (25a) to 87% (25c) and from $<1 \text{ s}^{-1}$ (25a) to 47.5 s^{-1} (25c), respectively. According to DFT analysis, the two-electron reduced species of 25 can exist as an open-shell singlet species as $\text{Ni}(\text{i})\text{L}^{\cdot-}$ for 25a or $\text{Ni}(\text{ii})\text{L}^{2\cdot-}$ for 25c. Further reduction of a $\text{Ni}(\text{i})$ center may lead to the formation of $\text{Ni}(\text{ii})\text{-H}$ in the presence of a proton.

In 2019, the Kubiak group reported the square planar nickel(II) complex $[(\text{bis-NHC})\text{Ni}(\text{dmpe})](\text{PF}_6)_2$ (26) by employing both bis-NHC ligand (bis-NHC = 3,3'-bis(1,3-propanediyl)dibenzimidazolin-2,2'-diylidene) and dmpe (1,2-bis(dimethylphosphino)ethane).⁹⁷ Prior to this work, nickel complexes supported by two diphosphine ligands were explored revealing the formation of nickel hydrides. The hydricity of these complexes was insufficient to effectively reduce CO_2 .^{98,99} By incorporating carbene donors, however, a concerted two-electron reduction of the nickel center was achieved at a relatively positive reduction potential of -1.87 V vs. Fc/Fc^+ . Consequently, 26 demonstrated electrocatalytic CO_2 reduction at an operating potential of -1.75 V, which is more positive than that of 25a-c, but it suffered from a relatively low CO production with a FE of 25%, due to substantial hydrogen evolution ($\text{FE}_{\text{H}_2} = 55\%$). Interestingly, the combination of phosphine and carbene donors creates a unique electronic environment around the nickel, enhancing its reducing power for CO_2 reduction. After recognizing that nickel complexes with both aliphatic and aromatic nitrogen donors (21–24) could catalyze the conversion of CO_2 to CO, the nickel catalyst was further optimized by introducing



carbene donors, as seen in **25a–c**, which showed improved performance. Due to the strong σ -donation, however, the operating potentials for CO_2 reduction in these complexes were too negative, ranging from -2.2 V to -2.4 V vs. Fc/Fc^+ . Incorporation of a bis-phosphine ligand in **26** finally shifted the operating potential positively by over 400 mV, making it more favorable for CO_2 reduction.

More recently, the Zhang group employed both mono- and dinuclear nickel complexes (**27** and **28**) supported by a redox-active 1,10-phenanthroline backbone (H_2bphpp : 2,9-bis(5-*tert*-2-hydroxy-3-pyridylphenyl)-1,10-phenanthroline and H_2hbpp : 2,9-bis(5-*tert*-butyl-2-hydroxyphenyl)-1,10-phenanthroline).¹⁰⁰ Both species exhibited $\sim 90\%$ of FE to give CO production when operating at -2.20 V vs. Fc/Fc^+ in DMF. Notably, the electrocatalytic current and TOF of the dinuclear $\text{Ni}_2(\text{bphpp})$ species (**28**) are approximately 5 times greater than those for mono-nuclear $\text{Ni}(\text{hbpp})$ (**27**) (~ 2.8 mA and 20.5 s^{-1} for **28** vs. ~ 0.5 mA and 4.4 s^{-1} for **27**). These results suggest that the additional nickel ion within **28** plays a crucial role in the catalytic CO_2 reduction process, facilitating disproportionation to yield both CO and CO_3^{2-} .

6 Conclusions

This review examines the current status and recent advancements in the field of CODH model chemistry to enhance our understanding of the fundamental chemical principles underlying enzymatic organometallic transformations. Notably, the CO_2 -bound form of Ni,Fe-CODH features a Ni-COO-Fe metal-carbonate moiety, which involves a two-electron reduction process. The active site of CODH features three sulfur donors that support a Ni center, enabling it to shuttle between T-shaped and tetrahedral geometries upon CO and CO_2 binding. As a part of a Fe-S cluster, the unique iron (Fe_u) site facilitates electron transfer and stabilizes the reduced CO_2 substrate through Lewis acid-base interaction. This bimetallic Ni, Fe-mediated transformation presents an intriguing approach for the selective conversion of CO_2 to CO under ambient conditions, thus inspiring further synthetic model studies. In particular, $\text{Ni-CO}_2\text{-TM}$ complexes and related nickel electrocatalysts have been highlighted. It is noteworthy that Ni plays a crucial role in the biological CO_2/CO conversion, potentially due to the stability of a Ni-C bond, which likely drives selectivity towards CO generation over the formate generation, as a competing two-proton, two-electron reduction process. To achieve CO_2 reduction at low overpotential, the incorporation of secondary coordination spheres, Lewis acid interactions, and changes in the nickel's geometry may be essential. One of the most enigmatic aspects of CODH chemistry is the storage of two reducing equivalents within the Ni-Fe/S cluster before CO_2 binding. This may arise from Ni-H or Ni-Fe bonds, warranting further research on heterometallic $\text{Ni-CO}_2\text{-TM}$ model compounds to uncover the role of heterometals such as Fe_u . Future model studies varying metal geometry and electronic structure will not only provide critical chemical insights into the understanding of CODH active site chemistry but also

contribute to the development of advanced (electro)catalysts for selective CO generation.

Data availability

No primary research results, software or code have been included and no new data were generated or analysed as part of this review.

Author contributions

Y. C., J. C. and Y. L. are prepared the manuscript. All authors contributed to the discussion.

Conflicts of interest

There are no conflicts to declare.

Acknowledgements

This research was supported by the National Research Foundation of Korea (2018R1A5A1025208, 2020R1A2C3007364, 2022M3C1A3092056 to Y. L., 2024M3J5A1023902 to C. Y., RS-2023-00240996 to J. C.) and by Chonnam National University (2024-0405-01 to J. C.).

Notes and references

- CO_2 Emissions in 2022, IEA, IEA, Paris, 2023.
- International Energy Agency, *Putting CO_2 to Use: Creating Value From Emissions*, OECD, 2019.
- Y. Yang and J.-W. Lee, *Chem. Sci.*, 2019, **10**, 3905–3926.
- A. M. Appel, J. E. Bercaw, A. B. Bocarsly, H. Dobbek, D. L. DuBois, M. Dupuis, J. G. Ferry, E. Fujita, R. Hille, P. J. A. Kenis, C. A. Kerfeld, R. H. Morris, C. H. F. Peden, A. R. Portis, S. W. Ragsdale, T. B. Rauchfuss, J. N. H. Reek, L. C. Seefeldt, R. K. Thauer and G. L. Waldrop, *Chem. Rev.*, 2013, **113**, 6621–6658.
- Carbon Dioxide as Chemical Feedstock*, ed. M. Aresta, Wiley, 1st edn, 2010.
- E. Boutin, L. Merakeb, B. Ma, B. Boudy, M. Wang, J. Bonin, E. Anxolabéhère-Mallart and M. Robert, *Chem. Soc. Rev.*, 2020, **49**, 5772–5809.
- F.-Y. Gao, R.-C. Bao, M.-R. Gao and S.-H. Yu, *J. Mater. Chem. A*, 2020, **8**, 15458–15478.
- R. Francke, B. Schille and M. Roemelt, *Chem. Rev.*, 2018, **118**, 4631–4701.
- C. Costentin, M. Robert and J.-M. Savéant, *Acc. Chem. Res.*, 2015, **48**, 2996–3006.
- M. Can, F. A. Armstrong and S. W. Ragsdale, *Chem. Rev.*, 2014, **114**, 4149–4174.
- M. Inoue, I. Nakamoto, K. Omae, T. Oguro, H. Ogata, T. Yoshida and Y. Sako, *Front. Microbiol.*, 2019, **9**, 3353.
- H. S. Shafaat and J. Y. Yang, *Nat. Catal.*, 2021, **4**, 928–933.
- S. H. Newman-Stonebraker, T. J. Gerard and P. L. Holland, *Chem.*, 2024, **10**, 1655–1667.



14 J. Fesseler, J.-H. Jeoung and H. Dobbek, *Angew. Chem., Int. Ed.*, 2015, **54**, 8560–8564.

15 W. Gong, B. Hao, Z. Wei, D. J. Ferguson, T. Tallant, J. A. Krzycki and M. K. Chan, *Proc. Natl. Acad. Sci. U. S. A.*, 2008, **105**, 9558–9563.

16 J.-H. Jeoung and H. Dobbek, *Science*, 2007, **318**, 1461–1464.

17 C. Darnault, A. Volbeda, E. J. Kim, P. Legrand, X. Vernède, P. A. Lindahl and J. C. Fontecilla-Camps, *Nat. Struct. Mol. Biol.*, 2003, **10**, 271–279.

18 C. L. Drennan, J. Heo, M. D. Sintchak, E. Schreiter and P. W. Ludden, *Proc. Natl. Acad. Sci. U. S. A.*, 2001, **98**, 11973–11978.

19 H. Dobbek, V. Svetlitchnyi, L. Gremer, R. Huber and O. Meyer, *Science*, 2001, **293**, 1281–1285.

20 J. Cirera, P. Alemany and S. Alvarez, *Chem.-Eur. J.*, 2004, **10**, 190–207.

21 J. Ghannam, T. Al Assil, T. C. Pankratz, R. L. Lord, M. Zeller and W.-T. Lee, *Inorg. Chem.*, 2018, **57**, 8307–8316.

22 L. C. Lewis, J. A. Sanabria-Gracia, Y. Lee, A. J. Jenkins and H. S. Shafaat, *Chem. Sci.*, 2024, **15**, 5916–5928.

23 V. J. DeRose, J. Telser, M. E. Anderson, P. A. Lindahl and B. M. Hoffman, *J. Am. Chem. Soc.*, 1998, **120**, 8767–8776.

24 C. Y. Ralston, H. Wang, S. W. Ragsdale, M. Kumar, N. J. Spangler, P. W. Ludden, W. Gu, R. M. Jones, D. S. Patil and S. P. Cramer, *J. Am. Chem. Soc.*, 2000, **122**, 10553–10560.

25 Z. Hu, N. J. Spangler, M. E. Anderson, J. Xia, P. W. Ludden, P. A. Lindahl and E. Münck, *J. Am. Chem. Soc.*, 1996, **118**, 830–845.

26 P. Amara, J.-M. Mouesca, A. Volbeda and J. C. Fontecilla-Camps, *Inorg. Chem.*, 2011, **50**, 1868–1878.

27 A. Majumdar, *Dalton Trans.*, 2014, **43**, 12135–12145.

28 D. Evans, *Coord. Chem. Rev.*, 2005, **249**, 1582–1595.

29 S. Groysman and R. H. Holm, *Biochemistry*, 2009, **48**, 2310–2320.

30 S. T. Stripp, B. R. Duffus, V. Fourmond, C. Léger, S. Leimkühler, S. Hirota, Y. Hu, A. Jasniewski, H. Ogata and M. W. Ribbe, *Chem. Rev.*, 2022, **122**, 11900–11973.

31 K. M. Waldie, A. L. Ostericher, M. H. Reineke, A. F. Sasayama and C. P. Kubiak, *ACS Catal.*, 2018, **8**, 1313–1324.

32 K. Sordakis, C. Tang, L. K. Vogt, H. Junge, P. J. Dyson, M. Beller and G. Laurenczy, *Chem. Rev.*, 2018, **118**, 372–433.

33 W.-H. Wang, Y. Himeda, J. T. Muckerman, G. F. Manbeck and E. Fujita, *Chem. Rev.*, 2015, **115**, 12936–12973.

34 R.-Z. Liao and P. E. M. Siegbahn, *Inorg. Chem.*, 2019, **58**, 7931–7938.

35 R. Breglia, F. Arrigoni, M. Sensi, C. Greco, P. Fantucci, L. De Gioia and M. Bruschi, *Inorg. Chem.*, 2021, **60**, 387–402.

36 D. W. N. Wilson, M. S. Fataftah, Z. Mathe, B. Q. Mercado, S. DeBeer and P. L. Holland, *J. Am. Chem. Soc.*, 2024, **146**, 4013–4025.

37 V. C.-C. Wang, M. Can, E. Pierce, S. W. Ragsdale and F. A. Armstrong, *J. Am. Chem. Soc.*, 2013, **135**, 2198–2206.

38 C. Yoo, S. Oh, J. Kim and Y. Lee, *Chem. Sci.*, 2014, **5**, 3853–3858.

39 D. Sahoo, C. Yoo and Y. Lee, *J. Am. Chem. Soc.*, 2018, **140**, 2179–2185.

40 K. Lee, J. Choi, P. M. Graham and Y. Lee, *Bull. Korean Chem. Soc.*, 2022, **43**, 222–226.

41 S. A. Akhade, W. Luo, X. Nie, N. J. Bernstein, A. Asthagiri and M. J. Janik, *Phys. Chem. Chem. Phys.*, 2014, **16**, 20429–20435.

42 J. D. Froehlich and C. P. Kubiak, *J. Am. Chem. Soc.*, 2015, **137**, 3565–3573.

43 P. W. Jolly and G. Wilke, in *The Organic Chemistry of Nickel*, Elsevier, 1974, pp. 1–32.

44 J. Chen, S. Huang, J. Seravalli, H. Gutzman, D. J. Swartz, S. W. Ragsdale and K. A. Bagley, *Biochemistry*, 2003, **42**, 14822–14830.

45 M. Aresta, C. F. Nobile, V. G. Albano, E. Forni and M. Manassero, *J. Chem. Soc., Chem. Commun.*, 1975, 636–637.

46 M. Aresta and C. F. Nobile, *J. Chem. Soc., Dalton Trans.*, 1977, 708–711.

47 A. Dohring, P. W. Jolly, C. Kruger and M. J. Romão, *Z. Naturforsch., B*, 1985, **40**, 484–488.

48 A. Paparo and J. Okuda, *Coord. Chem. Rev.*, 2017, **334**, 136–149.

49 D. H. Gibson, *Chem. Rev.*, 1996, **96**, 2063–2096.

50 J. S. Anderson, V. M. Iluc and G. L. Hillhouse, *Inorg. Chem.*, 2010, **49**, 10203–10207.

51 R. Beck, M. Shoshani, J. Krasinkiewicz, J. A. Hatnean and S. A. Johnson, *Dalton Trans.*, 2013, **42**, 1461–1475.

52 B. M. Puerta Lombardi, C. Gendy, B. S. Gelfand, G. M. Bernard, R. E. Wasylisen, H. M. Tuononen and R. Roesler, *Angew. Chem., Int. Ed.*, 2021, **60**, 7077–7081.

53 *CRC Handbook of Chemistry and Physics*, ed. W. M. Haynes, CRC Press, 95th edn, 2014.

54 F. A. Van Broekhuizen, I. M. N. Groot, H. J. Fraser, E. F. Van Dishoeck and S. Schlemmer, *Astron. Astrophys.*, 2006, **451**, 723–731.

55 S. Wolff, V. Pelmenschikov, R. Müller, M. Ertegi, B. Cula, M. Kaupp and C. Limberg, *Chem.-Eur. J.*, 2024, **30**, e202303112.

56 Y.-E. Kim, J. Kim and Y. Lee, *Chem. Commun.*, 2014, **50**, 11458–11461.

57 C. Yoo and Y. Lee, *Chem. Sci.*, 2017, **8**, 600–605.

58 A. Paparo and J. Okuda, *J. Organomet. Chem.*, 2018, **869**, 270–274.

59 D. Oren, Y. Diskin-Posner, L. Avram, M. Feller and D. Milstein, *Organometallics*, 2018, **37**, 2217–2221.

60 I. Castro-Rodriguez, H. Nakai, L. N. Zakharov, A. L. Rheingold and K. Meyer, *Science*, 2004, **305**, 1757–1759.

61 T.-W. Chiou, Y.-M. Tseng, T.-T. Lu, T.-C. Weng, D. Sokaras, W.-C. Ho, T.-S. Kuo, L.-Y. Jang, J.-F. Lee and W.-F. Liaw, *Chem. Sci.*, 2016, **7**, 3640–3644.

62 U. Terranova, *JBIC, J. Biol. Inorg. Chem.*, 2021, **26**, 617–624.

63 C. Yoo, J. Kim and Y. Lee, *Organometallics*, 2013, **32**, 7195–7203.

64 K. J. Jonasson, A. H. Mousa and O. F. Wendt, *Polyhedron*, 2018, **143**, 132–137.

65 F. Schneck, J. Ahrens, M. Finger, A. C. Stückl, C. Würtele, D. Schwarzer and S. Schneider, *Nat. Commun.*, 2018, **9**, 1161.

66 P. Zimmermann, S. Hoof, B. Braun-Cula, C. Herwig and C. Limberg, *Angew. Chem., Int. Ed.*, 2018, **57**, 7230–7233.

67 P. Zimmermann, D. Ar, M. Rößler, P. Holze, B. Cula, C. Herwig and C. Limberg, *Angew. Chem., Int. Ed.*, 2021, **60**, 2312–2321.

68 C. H. Lee, D. S. Laitar, P. Mueller and J. P. Sadighi, *J. Am. Chem. Soc.*, 2007, **129**, 13802–13803.

69 C. Yoo and Y. Lee, *Angew. Chem., Int. Ed.*, 2017, **56**, 9502–9506.

70 D. Huang and R. H. Holm, *J. Am. Chem. Soc.*, 2010, **132**, 4693–4701.

71 M. Aresta, A. Dibenedetto, E. Quaranta, M. Lanfranchi and A. Tiripicchio, *Organometallics*, 2000, **19**, 4199–4207.

72 F. D'Accriscio, A. Ohleier, E. Nicolas, M. Demange, O. Thillary Du Boulay, N. Saffon-Merceron, M. Fustier-Boutignon, E. Rezabal, G. Frison, N. Nebra and N. Mézailles, *Organometallics*, 2020, **39**, 1688–1699.

73 C. S. Yeung and V. M. Dong, *J. Am. Chem. Soc.*, 2008, **130**, 7826–7827.

74 P. Mastorilli, G. Moro, C. F. Nobile and M. Latronico, *Inorg. Chim. Acta*, 1992, **192**, 189–193.

75 M. Aresta, E. Quaranta and I. Tommasi, *J. Chem. Soc., Chem. Commun.*, 1988, 450–452.

76 M. Aresta, R. Gobetto, E. Quaranta and I. Tommasi, *Inorg. Chem.*, 1992, **31**, 4286–4290.

77 I. Tommasi, M. Aresta, P. Giannoccaro, E. Quaranta and C. Fragale, *Inorg. Chim. Acta*, 1998, **272**, 38–42.

78 C. Yoo and Y. Lee, *Inorg. Chem. Front.*, 2016, **3**, 849–855.

79 T. I. Doukov, T. M. Iverson, J. Seravalli, S. W. Ragsdale and C. L. Drennan, *Science*, 2002, **298**, 567–572.

80 T. I. Doukov, L. C. Blasiak, J. Seravalli, S. W. Ragsdale and C. L. Drennan, *Biochemistry*, 2008, **47**, 3474–3483.

81 P. Wang, M. Bruschi, L. De Gioia and J. Blumberger, *J. Am. Chem. Soc.*, 2013, **135**, 9493–9502.

82 J. Ruickoldt, Y. Basak, L. Dominik, J.-H. Jeoung and H. Dobbek, *ACS Catal.*, 2022, **12**, 13131–13142.

83 J. Heo, C. R. Staples, C. M. Halbleib and P. W. Ludden, *Biochemistry*, 2000, **39**, 7956–7963.

84 P. Gotico, Z. Halime, W. Leibl and A. Aukauloo, *ChemPlusChem*, 2023, **88**, e202300222.

85 A. W. Nichols and C. W. Machan, *Front. Chem.*, 2019, **7**, 397.

86 B. D. Steffey, C. J. Curtis and D. L. DuBois, *Organometallics*, 1995, **14**, 4937–4943.

87 J. Hawecker, J.-M. Lehn and R. Ziessel, *J. Chem. Soc., Chem. Commun.*, 1984, 328–330.

88 K. S. Ratliff, R. E. Lentz and C. P. Kubiak, *Organometallics*, 1992, **11**, 1986–1988.

89 M. D. Sampson, A. D. Nguyen, K. A. Grice, C. E. Moore, A. L. Rheingold and C. P. Kubiak, *J. Am. Chem. Soc.*, 2014, **136**, 5460–5471.

90 M. Beley, J.-P. Collin, R. Ruppert and J.-P. Sauvage, *J. Chem. Soc., Chem. Commun.*, 1984, 1315–1316.

91 J. D. Froehlich and C. P. Kubiak, *Inorg. Chem.*, 2012, **51**, 3932–3934.

92 F. Greenwell, B. Siritanaratkul, P. K. Sharma, E. H. Yu and A. J. Cowan, *J. Am. Chem. Soc.*, 2023, **145**, 15078–15083.

93 T. Qiu, G. P. A. Yap and J. Rosenthal, *ACS Appl. Energy Mater.*, 2019, **2**, 8560–8569.

94 V. V. Pavlishchuk and A. W. Addison, *Inorg. Chim. Acta*, 2000, **298**, 97–102.

95 L. E. Lieske, A. L. Rheingold and C. W. Machan, *Sustain. Energy Fuels*, 2018, **2**, 1269–1277.

96 X. Su, K. M. McCardle, J. A. Panetier and J. W. Jurss, *Chem. Commun.*, 2018, **54**, 3351–3354.

97 A. L. Ostericher, T. M. Porter, M. H. Reineke and C. P. Kubiak, *Dalton Trans.*, 2019, **48**, 15841–15848.

98 D. E. Berning, B. C. Noll and D. L. DuBois, *J. Am. Chem. Soc.*, 1999, **121**, 11432–11447.

99 C. J. Curtis, A. Miedaner, W. W. Ellis and D. L. DuBois, *J. Am. Chem. Soc.*, 2002, **124**, 1918–1925.

100 Y. Xiao, F. Xie, H.-T. Zhang and M.-T. Zhang, *JACS Au*, 2024, **4**, 1207–1218.

